

# Gas Slug Microfluidics: A Unique Tool for Ultrafast, Highly Controlled Growth of Iron Oxide Nanostructures

Ane Larrea,<sup>†</sup> Victor Sebastian,<sup>\*,†,‡</sup> Alfonso Ibarra,<sup>§</sup> Manuel Arruebo,<sup>†,‡</sup> and Jesus Santamaria<sup>\*,†,‡</sup>

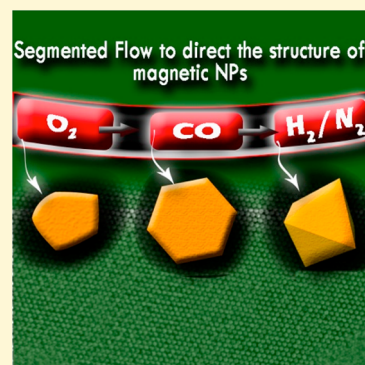
<sup>†</sup>Department of Chemical Engineering, Aragon Institute of Nanoscience (INA), University of Zaragoza, Campus Río Ebro-Edificio I+D, C/Poeta Mariano Esquillor S/N, 50018 Zaragoza, Spain

<sup>‡</sup>Networking Research Center on Bioengineering, Biomaterials and Nanomedicine, CIBER-BBN, 28029 Madrid, Spain

<sup>§</sup>Laboratorio de Microscopias Avanzadas (LMA), Universidad de Zaragoza, 50018 Zaragoza, Spain

## Supporting Information

**ABSTRACT:** The use of nanomaterials in real life applications is often hampered by our inability to produce them in large quantities while preserving their desired properties in terms of size, shape, and crystalline phase. Here we present a novel continuous method to synthesize nanostructures with an unprecedented degree of control regarding their properties. In particular, the excellent properties of microreactors for chemical synthesis are enhanced by the introduction of gas slugs of tailored composition. Slug dynamics accelerate mixing, reduce processing times (from hours in batch processes to minutes or even seconds), and, depending on the gas atmosphere used, allows one to accurately control the crystalline phase and shape of the resulting nanostructures. Inert ( $N_2$ ), oxidizing ( $O_2$ ), or reducing ( $CO$ ,  $H_2$ ) gases were used, leading to different morphologies and crystalline structures in a high yield, highly reproducible fabrication process.



## INTRODUCTION

The development of synthetic methods that afford a very precise control over the characteristics of magnetic nanoparticles (MNPs) remains a challenge in spite of intense research efforts in recent years.<sup>1</sup> This level of control is required to govern key nanoparticle properties such as particle size, bulk and surface composition, crystallinity, and colloidal stability that, in turn, will determine their success in a wide variety of potential applications. MNPs present unique properties in terms of chemical stability, size-dependent magnetic response, high surface to volume ratio, biocompatibility, and low price, which make them ideal candidates in biomedicine-related applications: drug delivery, hyperthermia, magnetic resonance imaging (MRI), tissue engineering and repair, biosensing, and biochemical separations.

The main synthesis pathways for the preparation of MNPs comprise physical, wet-chemical and microbial-based methods.<sup>1</sup> Wet-chemical methods are generally considered the most efficient since a high control on crystallinity and physicochemical properties can be achieved. However, a number of problems remain, which complicate the synthesis process and make it difficult to obtain a homogeneous product with the desired characteristics. Thus, this route often involves the use of surfactants to facilitate the formation of microemulsions to direct the synthesis to the desired shape and size, high temperature when using solvothermal processes, a strict pH control when using precipitation techniques, and a controlled atmosphere to promote the formation of a specific magnetic phase. High temperatures lead to rapid nucleation and growth

of the newly formed magnetic nanoparticles, which in turn requires an extremely fast reactant mixing to obtain monodisperse and pure nanomaterials. Also, the lack of control during mixing and heat transfer promotes heterogeneity regarding sizes, shapes, and magnetic phases. The strict conditions required during the synthesis of MNPs pose serious challenges for their mass production, and therefore new and reproducible synthetic approaches able to produce homogeneous, biocompatible, and functionalizable MNPs at industrial scale rates are highly desirable.<sup>2</sup>

Magnetite ( $Fe_3O_4$ ) is the most commonly used MNP in the biomedical field on account of its high saturation magnetization, biocompatibility, and easy surface functionalization to promote active targeting.<sup>3,4</sup> Besides magnetite, another interesting magnetic nanomaterial is feroxyhyte ( $\delta$ -FeOOH), a layered magnetic nanomaterial with high specific surface area and a large amount of surface hydroxyl groups available for targeted functionalization and adsorption.<sup>5</sup> Feroxyhyte is used as a magnetic sorbent for the removal of toxic ions from wastewater,<sup>6</sup> as a photocatalyst for water splitting,<sup>7</sup> and as a precursor for high coercive materials.<sup>8</sup> Recently, it has also been considered as a promising candidate for the next generation of spintronics.<sup>9</sup>

Microfluidic systems are a powerful tool to perform a wide range of chemical reactions.<sup>10</sup> Thus, compared to conventional

Received: January 22, 2015

Revised: March 12, 2015

Published: March 16, 2015

batch synthesis strategies, microfluidic systems allow a precise control of the reaction conditions (reaction time, temperature, reactant concentration, and stoichiometry), and their high surface-area-to-volume ratios and mixing characteristics help to reduce or avoid temperature and concentration inhomogeneities. This reduces polydispersity and guarantees the desired composition and crystal structure. Because of the control and reproducibility of physicochemical properties afforded by microfluidic systems, they are considered as the technology of choice in many processes for mass production of nanomaterials.<sup>2</sup> Particularly interesting is the concept of a gas–liquid segmented microreactor, where a fast and efficient mixing takes place in the liquid slugs between the homogeneously distributed gas segments.<sup>11–15</sup>

The synthesis of magnetic nanoparticles in a capillary-based droplet reactor has been previously demonstrated.<sup>16</sup> Under continuous or segmented flows it is possible to obtain magnetite nanoparticles with a narrow particle size distribution using a flow injection system.<sup>17</sup> Also, using coaxial flow millimeter-sized channels, Hassan et al.<sup>18</sup> were able to obtain superparamagnetic magnetite nanoparticles in a co-precipitation reaction. However, there is a wealth of opportunities to be exploited regarding the role of the gas used for the flow segmentation (inert, oxidant, or reductant) that to the best of our knowledge has not been studied. Indeed, the gas slugs can be regarded as mobile reservoirs from which one of the reactants can be efficiently supplied to the liquid phase.

Here we show that, by controlling the atmosphere in the gas segments, the crystalline phase and size of the resulting nanoparticles can be accurately tuned. We have been able to obtain pure magnetic phases of monodispersed crystalline MNPs in less than 2 min of reaction time. In addition, the synthesis method presented here produces MNPs that are easily dispersed in water and remain stably coated with lysine, a biocompatible amino acid.

## ■ EXPERIMENTAL SECTION

**Chemicals.** Potassium nitrate ( $\geq 99\%$ , KNO<sub>3</sub>, Fluka), ferrous sulfate heptahydrate ( $\geq 99\%$ , FeSO<sub>4</sub>·7H<sub>2</sub>O, Aldrich), sodium hydroxide ( $\geq 98\%$ , NaOH, Aldrich), L-lysine crystallized ( $\geq 98\%$ , C<sub>6</sub>H<sub>14</sub>N<sub>2</sub>O<sub>2</sub>, Aldrich), and sulfuric acid (95–98%, H<sub>2</sub>SO<sub>4</sub>, Aldrich) were used as received without further purification.

**Synthesis of Lysine–Fe<sub>3</sub>O<sub>4</sub> MNPs: Batch and Continuous Processes.** The synthesis protocol used was based on the well-known oxidative hydrolysis reported elsewhere<sup>1</sup> but with modification of the stabilizing agent in order to promote the MNP biocompatibility as briefly described here. The iron salt, FeSO<sub>4</sub>, was precipitated in basic media (NaOH) with a mild oxidant (KNO<sub>3</sub>). In the batch synthesis approach with the aid of a mechanical mixer, a 40 mL solution of 0.1 M KNO<sub>3</sub>, 90 mM NaOH, and 1 mM of L-lysine was prepared using deionized water. Afterward, this solution was bubbled with argon during 15 min to remove any trace of oxygen. Subsequently, 4.4 mL of an aqueous solution containing 65 mM FeSO<sub>4</sub>·7H<sub>2</sub>O and 17 mM of H<sub>2</sub>SO<sub>4</sub> was added dropwise under constant stirring. When the addition was completed, argon was allowed to pass for another 15 min and the suspension was heated at 90 °C for 1 h in an oil bath.

In the continuous synthesis approach, solutions were prepared as follows. In a 60 mL vessel (solution 1), a solution consisting of 180 mM KNO<sub>3</sub>, 162 mM NaOH, and 1.85 mM L-lysine was prepared. Solution 2 was composed of the following: 60 mL of deionized water, 13 mM ferrous sulfate heptahydrate, and 3.38 mM sulfuric acid. Argon was bubbled in each solution for 15 min. After deoxygenation, each solution was placed in 60 mL plastic Becton Dickinson syringes. Solutions 1 and 2 were injected at a proper flow rate to obtain the desired residence time according to the microfluidic system volume. Solutions 1 and 2 streams were mixed in a PEEK polymer Y-junction

under a constant flow ratio of 1:1 in order to ease the synthesis procedure. The microfluidic system is composed of two PTFE coils (1/16 in. o.d. and 0.04 in. i.d.) which are conceived as mixing and reaction stages, respectively.

Mixing by sonication was carried out by setting the mixing poly(tetrafluoroethylene) (PTFE) coil in an ultrasonic bath, maintaining the bath temperature in the range between 25 and 30 °C using a cooling bath. Finally, a new modification from the previous approach was established, adding a pure gas (N<sub>2</sub>, H<sub>2</sub>, O<sub>2</sub>, and CO) stream after the mixing coil to obtain a stable gas–liquid segmented flow in the reaction stage. The temperature at the reaction stage was varied from 70 to 110 °C. Experiments with a synthesis temperature higher than 90 °C were carried out by maintaining the reactor pressure at 1.4 bar. The synthesized nanoparticles were centrifuged at 10,000 rpm for 10 min, then washed twice with distilled water, and finally resuspended in distilled water.

Equation 1 gives the mixing time as a function of the tubing diameter or channel width ( $d$ ) and the diffusion coefficient of ions into the aqueous solution ( $D$ ) roughly estimated<sup>19</sup> at  $10^{-9}$  m<sup>2</sup>·s<sup>-1</sup>. From eq 1 (the effect of chemical reactions was not considered), the time ( $\tau_{\text{mix}}$ ) required for the complete mixing of the two inlet streams was estimated at 60 s.

$$\tau_{\text{mix}} = \frac{d_t^2}{4D} \quad (1)$$

**Powder X-ray Diffraction.** The phases of iron oxide nanoparticles were identified by powder X-ray diffraction (XRD). The X-ray patterns were collected between 20° and 80° ( $2\theta$ ) in a D-Max Rigaku diffractometer with Cu K $\alpha$  radiation.

**Transmission Electron Microscopy–High Resolution Transmission Electron Microscopy.** The particle morphology and size distribution have been determined at the Advanced Microscopy Laboratory (LMA), Instituto Universitario de Nanociencia de Aragón (INA), Zaragoza, Spain, by a FEI Tecnai thermionic transmission electron microscopy (TEM) operated at 200 kV. At least 200 particles were measured to evaluate the mean diameter of the particles (DTEM) and distribution. High resolution transmission electron microscopy (HRTEM) was performed to determine the morphology and the crystalline structure, using a FEI Tecnai field emission gun operated at 300 kV and FEI Cs-image corrected (60–300 kV) TEM operated at 300 kV. To prepare the sample, the nanoparticle suspension was diluted with ethanol and sonicated for 30 s before the casting of 5  $\mu$ L on a lacey carbon TEM grid.

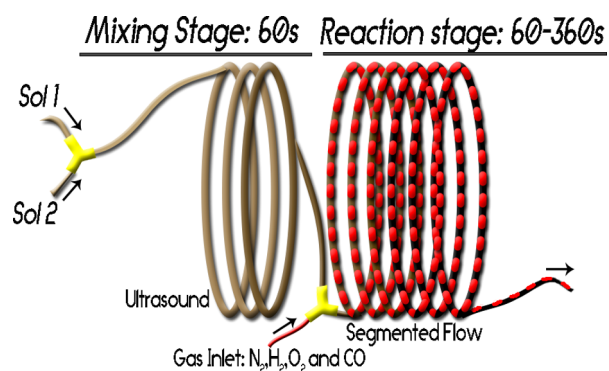
**Magnetometer.** The magnetic properties of the different nanoparticles were measured as dried powders after solvent evaporation at different temperatures in a superconducting quantum interference device (SQUID MPMS-5S, Quantum Design) from 0 to 40000 Oe. The samples were measured in a gelatin capsule (a diamagnetic correction for the sample holder was carried out). Magnetic hysteresis loops (plot of the magnetization of the sample as a function of the magnetic field strength) were evaluated at 37 °C. Zero-field-cooled and field-cooled (500 Oe) curves were measured from 5 to 315 K. Magnetic-moment values are given per unit of total mass (emu/g), that is, considering the total mass of both magnetite and capping agent (lysine).

**Determination of Iron content.** Iron content was determined by microwave plasma-atomic emission spectrometry (Agilent 4100 MP-AES). Samples were digested with the addition of nitric acid (HNO<sub>3</sub>) and hydrochloric acid (HCl) in a volume ratio of 1:3; the mixture was heated at 65 °C during 2 h. The resultant digestion was diluted with Milli-Q water to a final volume of 25 mL for spectrometric analysis.

## ■ RESULTS

In the microfluidic system here described, two aqueous solutions were mixed in a Y-junction (500  $\mu$ m inside diameter). Two microfluidic sections were used (Scheme 1): In stage 1 the mixing of precursors at room temperature took place with 60 s residence time (this time was estimated according to fluid-

**Scheme 1. Microfluidic Setup Designed To Produce MNPs in Continuous Gas–Liquid Segmented Flow<sup>a</sup>**



<sup>a</sup>The mixing stage is irradiated by ultrasound waves, and the reaction stage is where gas–liquid slugs direct the crystallization of different magnetic nanostructures.

dynamic parameters;<sup>19</sup> see the Supporting Information (SI)), while in stage 2 oxidative hydrolysis was performed at temperatures between 70 and 110 °C under different residence times. The mixing stage was irradiated with ultrasound waves to control the formation of aggregates and narrow the residence time distribution of the resulting MNPs. This approach avoided the formation of micrometric size aggregates.

#### Inert Gas Slugs: Nitrogen–Liquid Segmented Flow.

The synthesis of magnetite ( $Fe_3O_4$ ) is usually performed under an inert atmosphere to prevent the oxidation and subsequent transformation of the spinel into maghemite ( $\gamma-Fe_2O_3$ ) in contact with air.<sup>20,21</sup> Considering that the microfluidic reactor made of PTFE is slightly permeable to oxygen,<sup>22</sup> we have introduced nitrogen–liquid segmented flow to prevent the oxidation of magnetite during the continuous production. Although the surface of the microfluidic reactor in this work is hydrophobic, the aqueous phase is still the continuous phase. The slug length is an important hydrodynamic parameter, since it has a very significant effect on the gas–liquid mass transfer. The length of the slugs and also the grade of mixing generated by the internal circulation depend on the gas and liquid volumetric flow rates.<sup>13</sup> At short residence times, small slugs and good mixing are obtained.<sup>13</sup> A hydrophobic reactor surface was selected for this synthesis to avoid MNPs nucleation on the reactor walls, thus preventing reactor fouling and uncontrolled particle growth. The liquid–gas volume flow ratio was kept constant at a value of 1 in order to form small slugs that enable a strong recirculation, characterized by a high vorticity, enhancing the gas transfer to the liquid slug during the reaction stage. Figure 1a shows the uniform, segmented slugs generated at the inlet of the reaction stage. As the liquid slugs moved through the reaction stage, their color darkened, turning into black, indicating that  $Fe^{2+}$  ions are transforming into MNPs.

The study on the influence of the residence time and temperature at the reaction stage revealed that a pure phase of magnetite could be only obtained at temperatures above 100 °C (Figure 1b and Figure S1 in the SI). A residence time shorter than 6 min, (calculated considering both the gas and liquid flow rates) or a temperature lower than 100 °C gave rise to a mixture of octahedral and laminar-shaped nanocrystals which correspond with magnetite and iron(III) hydroxides<sup>5,20</sup> (Figure S1 in the SI).

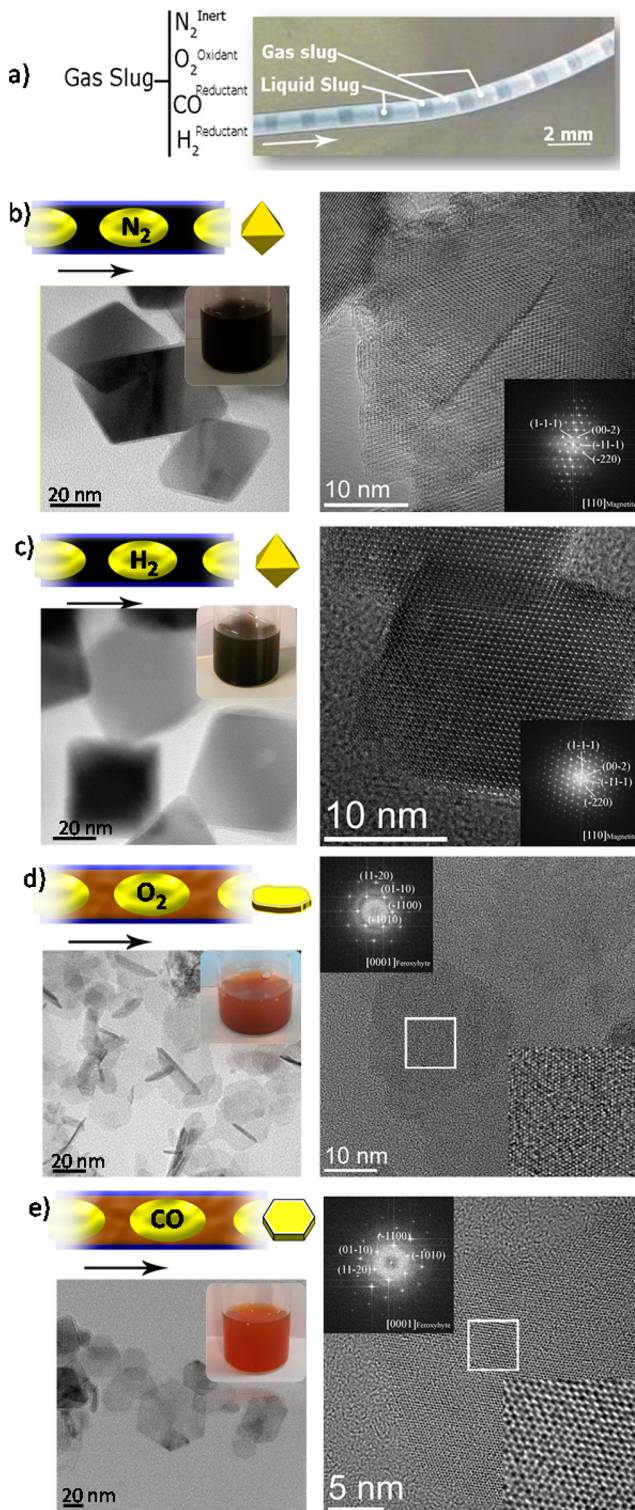


**Figure 1.** | Magnetic nanomaterials produced by the liquid segmentation of reagents with different gas sources: (a) optical image of the gas–liquid slug for different gas phase compositions in the segmented flow; (b–d) TEM images of MNPs obtained under different gas atmospheres, optical images of colloids (insets), HRTEM images, and FFT [(b)  $N_2$ , 100 °C, and 6 min; (c)  $H_2$ , 100 °C, and 1 min; (d)  $O_2$ , 100 °C, and 1 min; (e)  $CO$ , 80 °C, and 1 min]. White squares indicate the area selected for the high magnification inset.

The residence time required to obtain pure magnetite decreased when the reaction temperature was set above 100 °C,

but the size distribution was not as narrow as at 100 °C. These results could be related to the modification of the nucleation and crystallization rates, as well as to the presence of an accused Ostwald ripening process since both the average particle size and the width of the size distribution were smaller at lower temperatures (Figure S1 in the SI). In fact, Baumgartner et al.<sup>23</sup> demonstrated that nucleation and growth of magnetite proceed through a rapid agglomeration of primary particles of nanometric size. The strong decrease of the time required for a complete transformation of Fe<sup>2+</sup> ions in Fe<sub>3</sub>O<sub>4</sub> spinel MNPs by the hydration of the intermediate ferric and ferrous hydroxides<sup>24</sup> can be credited to the enhancement of the heat and mass transfer processes in the microfluidic system, leading to faster nucleation–growth processes.

### Reducing Gas Slugs: Hydrogen–Liquid Segmented Flow.

It has been reported that, in the production of iron oxides from ferrous salts,<sup>25</sup> the presence of NO<sup>3-</sup> ions at a basic pH contributes to the oxidation of Fe(OH)<sub>2</sub> hydroxides to FeOOH and the subsequent formation of magnetite. However, the presence of hydrogen can also promote the reduction of iron(III) hydroxides to magnetite,<sup>25</sup> accelerating the production and increasing the yield to magnetite. Therefore, introducing H<sub>2</sub> in the gas slugs of the segmented flow seems a promising alternative to enhance the formation of magnetite at synthesis conditions where this could not be obtained under nitrogen. Parts b and c of Figure 1 show that magnetite nanocrystals with their characteristic octahedral shape were obtained with both N<sub>2</sub> and H<sub>2</sub> slugs under segmented flow. Indeed the strong and sharp diffraction peaks in the XRD patterns obtained with N<sub>2</sub> and H<sub>2</sub> slug flow at the optimum conditions, as well as the electron diffraction analysis (Figure 2a,b), correspond to the face-centered-cubic phase of Fe<sub>3</sub>O<sub>4</sub> (JCPDS No. 19-0629; Figure 3). However, the presence of H<sub>2</sub> was able to accelerate the reaction to the point that the formation of a pure phase of

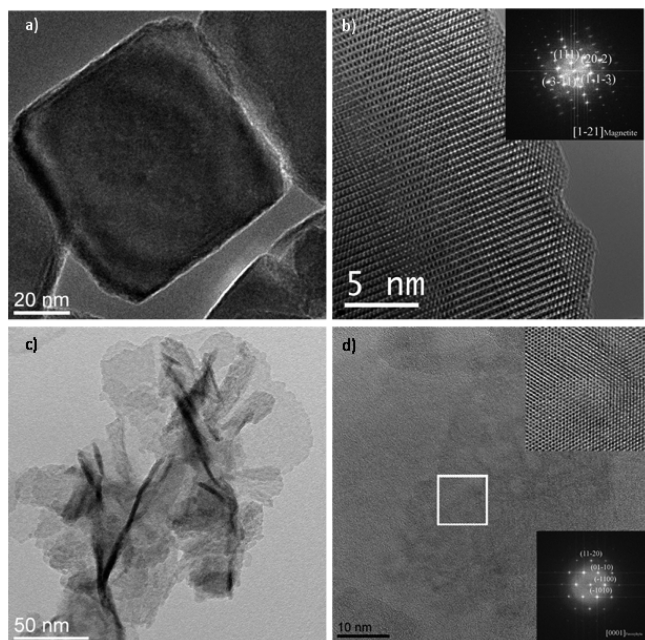


**Figure 2.** | Electron diffraction analysis performed by HR-TEM and FFT showing that (a, b) the octahedral-shaped nanoparticles correspond with the Fe<sub>3</sub>O<sub>4</sub> spinel structure ( $Fd\bar{3}m$ ;  $a = 8.397 \text{ \AA}$ ) and (c, d) the layered nanoparticles correspond with the feroxyhyte ( $\delta$ -FeOOH;  $P\bar{3}m1$ ;  $a = 2.93 \text{ \AA}$ ;  $c = 4.6 \text{ \AA}$ ) structure.

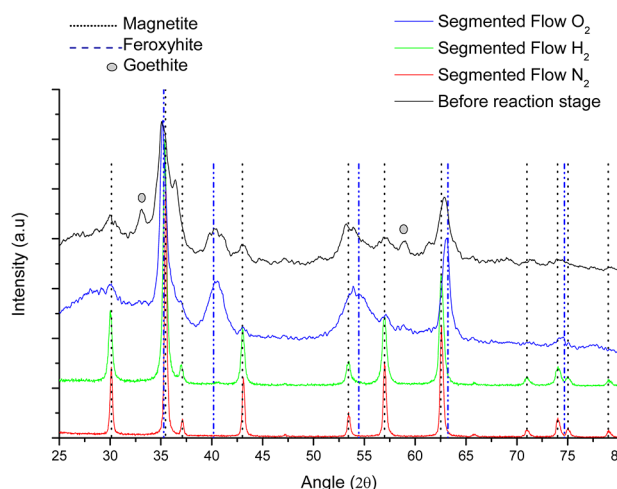


**Figure 3.** | X-ray powder diffraction patterns of MNPs obtained under gas–liquid segmentation, with O<sub>2</sub>, H<sub>2</sub>, and N<sub>2</sub>, and for nanoparticles collected after the mixing stage.

magnetite, without the presence of iron(III) hydroxides, was achieved at 100 °C under a residence time of only 60 s (Figure S2 of the SI). This means that the production rate of magnetite could be increased 6-fold in comparison with N<sub>2</sub> slug flow and the presence of impurities was avoided just by modifying the gas phase reaction environment.

### Oxidizing Gas Slugs: Oxygen–Liquid Segmented Flow.

To confirm the extraordinary influence of the nature of the segmented gas in the crystallization of MNPs, oxygen was injected instead of N<sub>2</sub> and H<sub>2</sub>, while maintaining the same synthesis parameters as well as precursor composition. In this case, an orange dispersion was obtained instead of a black one, confirming that a phase different from magnetite had been obtained (Figure 1d). TEM characterization showed that the presence of O<sub>2</sub> promotes the growth of irregular-shaped MNPs that could be described as nanoflakes with a mean size (along the longest axis) of about  $30 \pm 8$  and 3 nm thickness (Figure 1d). Electron diffraction (Figure 2c,d) and XRD (Figure 3) analyses confirmed that pure crystalline iron(III) MNPs were obtained, with a crystalline structure corresponding to feroxyhyte ( $\delta$ -FeOOH), which is usually obtained from ferrous salts in the presence of H<sub>2</sub>O<sub>2</sub>.<sup>25</sup> The oxidized spinel (maghemite) phase was absent from the XRD patterns (Figure 3). Only feroxyhyte was obtained under highly oxidizing conditions. This means that, under fast mass transfer conditions, O<sub>2</sub> can replace hydrogen peroxide as the oxidant employed in feroxyhyte synthesis<sup>5,25</sup> promoting the formation of a new magnetic phase instead of forming maghemite ( $\gamma$ -Fe<sub>2</sub>O<sub>3</sub>) from the oxidation of the spinel phase. The main source for the observed broadening of the XRD peaks could be attributed to the narrowing of feroxyhyte in the direction (001), which corresponds to the interlayer stacking direction, and is consistent with the platelet shape of diffracting domains.<sup>26</sup> This was also confirmed by ultra-HRTEM characterization (Figure 2c,d).

**Early Reaction Stages with O<sub>2</sub> and H<sub>2</sub> Slugs.** Microfluidic reactors also represent a suitable tool to study the mechanism of nanomaterial synthesis in a time scale of a few seconds.<sup>13</sup> To investigate the formation of magnetite and feroxyhyte at short contact times without modifying the geometrical characteristics of the reactor (and therefore the fluid dynamics), an interface with several outlet stages was

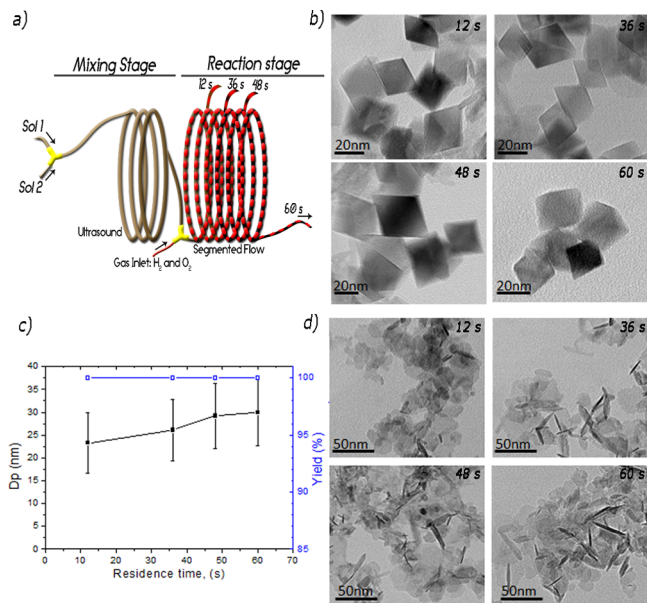


**Figure 4.** | Early reaction stage characterization: (a) scheme of the microfluidics setup designed to study MNPs production in continuous flow at residence times shorter than 60 s and under O<sub>2</sub> and H<sub>2</sub> gas–liquid slug flow; (b) TEM images of MNPs obtained under H<sub>2</sub> gas atmosphere at 12, 36, 26, and 60 s; (c) particle size distribution for MNPs obtained under H<sub>2</sub> gas atmosphere and yield of MNPs production; (d) TEM images of MNPs obtained under O<sub>2</sub> gas atmosphere at 12, 36, 26, and 60 s.

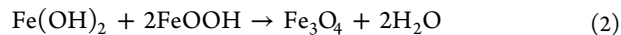
implemented. After reaching steady state, the different corresponding outlet channels were sampled sequentially in the direction of decreasing reaction times (Figure 4a). This provided valuable insight on the crystallization phenomena and kinetics at short reaction times while avoiding disturbances in the process. Figure 4b shows the morphology and dimensions of Fe<sub>3</sub>O<sub>4</sub> spinel nanocrystals at 12, 36, 48, and 60 s of reaction time. It must be highlighted that the octahedral shape of the spinel nanocrystals was already present even at the shortest of the residence times tested (12 s); however, the particle size increased with residence time from 23 ± 6 to 28 ± 7 nm at 12 and 60 s, respectively (see Figure 4c and SI Figure S3). These observations support a mechanism in which a rapid nucleation takes place initially, and most of the residence time in the reactor is used to grow the crystals formed, with few or no additional nucleation events. In fact, the elemental analysis of the surrounding liquid revealed that complete conversion of the iron precursor was achieved already after the first reaction section (12 s residence time). Figure 3 shows the diffractogram of the nanomaterials produced after the co-precipitation at the mixing stage. The metastable phase is mainly composed of iron hydroxides (goethite and feroxyhyte) as well as magnetite.

These results are consistent with the TEM images, where a wide variety of nanoparticles with heterogeneous shape, ranging from nanosheets to nanobars and octahedral are depicted (Figure S4 in the SI). The same mechanism and evidence were found when O<sub>2</sub> was used as segmented gas instead of H<sub>2</sub>, but a clear assessment of the resulting feroxyhyte particle dimensions was difficult to obtain owing to the fact that the nanoplates strongly aggregate after drying on the TEM grid. The depletion of Fe precursors in the growing solution also confirms a nearly instantaneous nucleation. This process sequesters iron species into the metastable particles that are then rapidly transformed

into the most stable form at the reaction temperature and gas environment.

### Oxidizing/Reducing Gas Slugs: CO–Liquid Segmented Flow.

Carbon monoxide is generally considered as a poisoning agent in many catalytic studies but is also considered as a reducing agent or even a capping agent to direct the shape control in nanoparticle synthesis.<sup>27</sup> The effect of the presence of CO during the synthesis of MNPs was studied by producing CO gas slugs using the same procedure described earlier for N<sub>2</sub>, H<sub>2</sub>, and O<sub>2</sub>. The analysis of the results obtained using CO slugs under experimental conditions reflects the dual role that CO may have on the crystallization of MNPs depending on the synthesis temperature. At temperatures lower than 80 °C, an orange dispersion was obtained, similar to that obtained in the presence of O<sub>2</sub> (Figure 1e). Electron diffraction analysis (Figure 1e) also confirmed that a pure and crystalline phase of feroxyhyte was produced under those conditions. Nevertheless the TEM microphotographs showed that the MNPs grew into hexagonal nanoplates with an average particle size of 70 ± 12 nm and thickness of 3 nm. It is therefore interesting to highlight that at low temperatures CO does not act as a reducing agent, as H<sub>2</sub> does, and instead directs the oxidation of iron hydroxides to feroxyhyte. In addition, the strong adsorption of CO to the Fe atoms<sup>28</sup> controls the shape of the feroxyhyte nanocrystals, leading to hexagonal nanoplates, i.e., acting mainly as a capping agent. At higher temperatures, the adsorption-capping route becomes less important and CO shifts to a predominantly reducing role. This is already noticeable at temperatures above 80 °C and short residence times, where a mixture of hexagonal nanoplates and octahedral nanoparticles is obtained. With a further increase of temperature to 100 °C, crystalline and pure magnetite nanoparticles were obtained at 1 min of residence time (Figure S5 in the SI). This is consistent with the results obtained in the presence of H<sub>2</sub>, and it would imply that under these conditions CO acts only as a reducing agent. The capping/reductant role transition is governed by adsorption processes at the MNP surface. It is reported that FeOOH nanoparticles are an active iron-based catalyst in the oxidation of CO at temperatures higher than 100 °C.<sup>29</sup> This is related to a weak adsorption of CO on the surface of FeOOH hydroxides, and when the temperature increases, FeOOH can easily release oxygen to oxidize the CO to CO<sub>2</sub>.<sup>29</sup> This explains also our observations: the CO adsorbed on the surface of FeOOH can be oxidized to CO<sub>2</sub> and iron(III) hydroxides can be partially reduced to Fe(II) to form magnetite (Fe<sub>3</sub>O<sub>4</sub>) according to



### Magnetic Properties and Synthesis Reproducibility.

The magnetic measurements carried out at different temperatures and the hysteresis loops for the resulting MNPs are shown in Figure 5. When using H<sub>2</sub> as the gas for the flow segmentation ( $D = 35$  nm), a clear ferromagnetic behavior was obtained with a saturation magnetization close to 72 emu/g (Figure 5a). This value is lower than the magnetic moments measured for bulk magnetite samples (92 emu/g), as expected due to the increased disorder at the particle surfaces as their size is decreased.<sup>30</sup> It must also be noted that magnetic-moment values are given per unit of total mass (emu/g), that is, considering the total mass of both magnetite and capping agent (lysine). In this case (inset in Figure 5a) a remanence of 8.4 emu/g and a coercivity of 80 Oe at 37 °C were found. The resulting magnetization is very similar to that of the particles

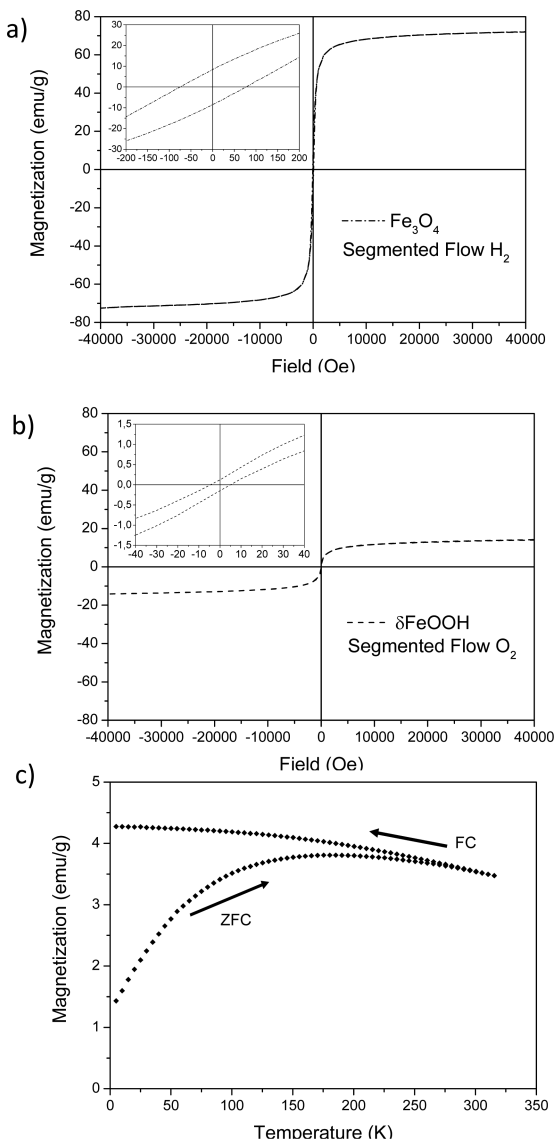


**Figure 5.** | Magnetic hysteresis diagrams (at 37 °C) of the magnetic nanoparticles produced in this work by using (a) the microfluidic reactor with H<sub>2</sub> flow segmentation ( $D = 35$  nm) and (b) the microfluidic reactor with O<sub>2</sub> flow segmentation; (c) the ZFC/FC plots for nanoparticles produced in the microfluidic reactor with O<sub>2</sub> flow segmentation.

produced in a batch reactor where a saturation magnetization of 84 emu/g, a remanence of 15 emu/g, and a coercivity of 115 Oe were obtained at 37 °C. However, the synthesis in the microreactor took place in a few seconds instead of the hour needed to complete the synthesis in the batch reactor. When O<sub>2</sub> was used (Figure 5b), a lower magnetization (14 emu/g at 4 T) was obtained and a clear superparamagnetic behavior (no remanence or coercivity) was observed. Those values are in agreement with the previous literature for the feroxyhyte.<sup>31</sup> Figure 5c shows also the zero-field-cooling (ZFC) and field-cooling plots ( $H = 500$  Oe), which corroborate the superparamagnetic behavior with a blocking temperature close to 180 K.

One major challenge for the scaled up synthesis of nanomaterials and nanoparticles is the reproducibility of the synthesis in terms of controlling the size and morphology of the resulting particles. The microfluidic synthesis of nanoparticles

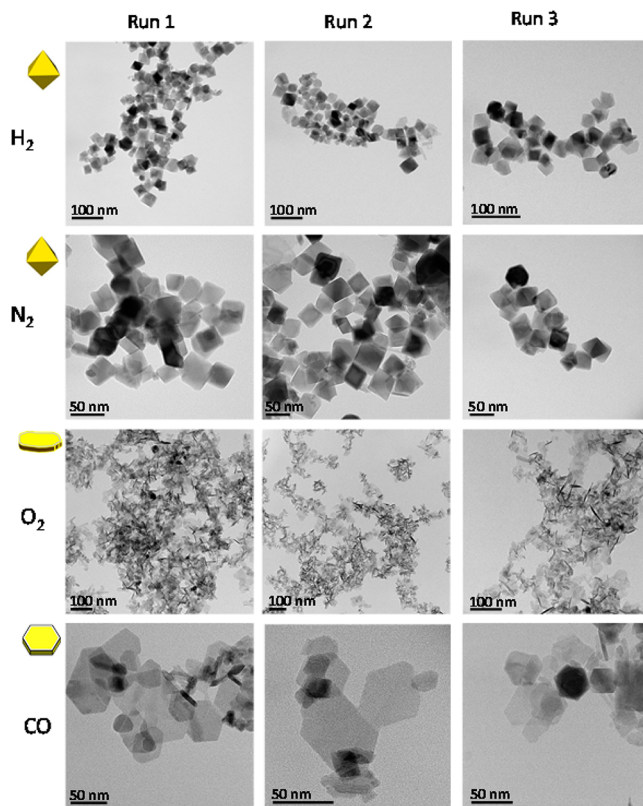


**Figure 6.** | Reproducibility study. TEM images of MNPs obtained at different runs under gas–liquid slug flow: H<sub>2</sub> and O<sub>2</sub> at 1 min and 100 °C, N<sub>2</sub> at 6 min and 100 °C, and CO at 1 min and 80 °C.

can enhance the controllability and reproducibility of the resulting nanoparticles compared to conventional batch methods<sup>32</sup> due to the fine control at the mixing and reaction levels. Figure 6 depicts representative TEM images of the MNPs obtained at different synthesis runs under the optimum conditions mentioned before. The synthesis of MNPs presents good reproducibility and comparable interbatch nanoparticle size distributions (Figure S6 in the SI). The robustness of the microfluidic reactor was studied by the analysis of the quality of the resulting nanoparticles at different time intervals. Figure S7 in the SI depicts an excellent reproducibility according to the morphology and size of the produced nanoparticles along the synthesis time (3 h), which demonstrates that microfluidics are excellent candidates to overcome irreproducibility of conventional batch reactors (Figure S8 in the SI).

## ■ CONCLUSION

In conclusion, the preceding results clearly show the potential of gas slug microfluidics as the system of choice to synthesize a variety of high purity, custom-made crystalline iron oxide nanostructures. Not only the productivity is enhanced by strongly reducing residence times with respect to the batch process (from hours to minutes or even seconds) but also a high degree of control over the resulting product characteristics (size, shape, crystalline phase) can be obtained by simply changing the composition of the gas used to create the slugs. Our results show that it is beneficial to segregate the mixing and reaction stages. A fast mixing is essential (since nearly all of the oxide precursors are removed from the liquid phase in less than a minute, leading to a fast nucleation process), followed by a reaction stage where the temperature and reaction atmosphere

are selected depending on the desired characteristics. This allows an accurate control on the final shape and size (and therefore on the properties) of the resulting products. Thus, gas slug microfluidics provide a flexible, easy to implement a process to produce customized iron oxide nanostructures.

## ■ ASSOCIATED CONTENT

### § Supporting Information

Figures showing TEM micrographs and particle size distributions of MNPs under various conditions and TEM images of iron oxide nanostructures. This material is available free of charge via the Internet at <http://pubs.acs.org>.

## ■ AUTHOR INFORMATION

### Corresponding Authors

\*(V.S.) E-mail: [victorse@unizar.es](mailto:victorse@unizar.es).

\*(J.S.) E-mail: [jesus.santamaria@unizar.es](mailto:jesus.santamaria@unizar.es).

### Notes

The authors declare no competing financial interest.

## ■ ACKNOWLEDGMENTS

The EU CIG-Marie Curie under the REA Grant Agreement No. 321642 and the ERC Consolidator Grant program (ERC-2013-CoG-614715, NANOHEDONISM) are gratefully acknowledged. A.I. thanks the Gobierno de Aragón (Grant E81) and Fondo Social Europeo.

## ■ REFERENCES

- (1) Reddy, L. H.; Arias, J. L.; Nicolas, J.; Couvreur, P. *Chem. Rev.* **2012**, *112*, 5818.
- (2) Sebastian, V.; Arruebo, M.; Santamaria, J. *Small* **2014**, *10*, 835.
- (3) Massart, R.; Cabuil, V. *J. Chim. Phys. Phys.-Chim. Biol.* **1987**, *84*, 967.
- (4) Jovanovic, S.; Spreitzer, M.; Otonicar, M.; Jeon, J. H.; Suvorov, D. *J. Alloys Compd.* **2014**, *589*, 271.
- (5) Cornell, R. M.; Schwertmann, U. *The Iron Oxides: Structure, Properties, Reactions, Occurrences and Uses*; Wiley-VCH: Weinheim, Germany, 2003.
- (6) Muller, K.; Ciminelli, V. S. T.; Dantas, M. S. S.; Willscher, S. *Water Res.* **2010**, *44*, 5660.
- (7) Pereira, M. C.; Garcia, E. M.; da Silva, A. C.; Lorencon, E.; Ardisson, J. D.; Murad, E.; Fabris, J. D.; Matencio, T.; Ramalho, T. D.; Rocha, M. V. J. *J. Mater. Chem.* **2011**, *21*, 10280.
- (8) Chin, T. S.; Deng, M. C.; Hsu, S. L. *Mater. Chem. Phys.* **1994**, *37*, 45.
- (9) Chen, P. Z.; Xu, K.; Li, X. L.; Guo, Y. Q.; Zhou, D.; Zhao, J. Y.; Wu, X. J.; Wu, C. Z.; Xie, Y. *Chem. Sci.* **2014**, *5*, 2251.
- (10) Marre, S.; Jensen, K. F. *Chem. Soc. Rev.* **2010**, *39*, 1183.
- (11) Nakamura, H.; Yamaguchi, Y.; Miyazaki, M.; Maeda, H.; Uehara, M.; Mulvaney, P. *Chem. Commun. (Cambridge, U. K.)* **2002**, 2844.
- (12) Gunther, A.; Jensen, K. F. *Lab Chip* **2007**, *7*, 399.
- (13) Cabeza, V. S.; Kuhn, S.; Kulkarni, A. A.; Jensen, K. F. *Langmuir* **2012**, *28*, 7007.
- (14) Khan, S. A.; Gunther, A.; Schmidt, M. A.; Jensen, K. F. *Langmuir* **2004**, *20*, 8604.
- (15) Gunther, A.; Khan, S. A.; Thalmann, M.; Trachsel, F.; Jensen, K. F. *Lab Chip* **2004**, *4*, 278.
- (16) Kumar, K.; Nightingale, A. M.; Krishnadasan, S. H.; Kamaly, N.; Wylenzinska-Arridge, M.; Zeissler, K.; Branford, W. R.; Ware, E.; deMello, A. J.; deMello, J. C. *J. Mater. Chem.* **2012**, *22*, 4704.
- (17) Salazar-Alvarez, G.; Muhammed, M.; Zagorodni, A. A. *Chem. Eng. Sci.* **2006**, *61*, 4625.
- (18) Abou Hassan, A.; Sandre, O.; Cabuil, V.; Tabeling, P. *Chem. Commun. (Cambridge, U. K.)* **2008**, 1783.
- (19) Nagy, K. D.; Shen, B.; Jamison, T. F.; Jensen, K. F. *Org. Process Res. Dev.* **2012**, *16*, 976.
- (20) Verges, M. A.; Costo, R.; Roca, A. G.; Marco, J. F.; Goya, G. F.; Serna, C. J.; Morales, M. P. *J. Phys. D Appl. Phys.* **2008**, *41*, No. 134003.
- (21) Calatayud, M. P.; Riggio, C.; Raffa, V.; Sanz, B.; Torres, T. E.; Ibarra, M. R.; Hoskins, C.; Cuschieri, A.; Wang, L.; Pinkernelle, J.; Keilhoff, G.; Goya, G. F. *J. Mater. Chem. B* **2013**, *1*, 3607.
- (22) Gomez, L.; Sebastian, V.; Irusta, S.; Ibarra, A.; Arruebo, M.; Santamaria, J. *Lab Chip* **2014**, *14*, 325.
- (23) Baumgartner, J.; Dey, A.; Bomans, P. H. H.; Le Coadou, C.; Fratzl, P.; Sommerdijk, N. A. J. M.; Faivre, D. *Nat. Mater.* **2013**, *12*, 310.
- (24) Iida, H.; Takayanagi, K.; Nakanishi, T.; Osaka, T. *J. Colloid Interface Sci.* **2007**, *314*, 274.
- (25) Correa, J. R.; Canetti, D.; Castillo, R.; Llopiz, J. C.; Dufour, J. *Mater. Res. Bull.* **2006**, *41*, 703.
- (26) Polyakov, A. Y.; Goldt, A. E.; Sorkina, T. A.; Perminova, I. V.; Pankratov, D. A.; Goodlin, E. A.; Tretyakov, Y. D. *CrystEngComm* **2012**, *14*, 8097.
- (27) Chen, M.; Wu, B. H.; Yang, J.; Zheng, N. F. *Adv. Mater.* **2012**, *24*, 862.
- (28) Allen, V. M.; Jones, W. E.; Pacey, P. D. *Surf. Sci.* **1989**, *220*, 193.
- (29) Li, P.; Miser, D. E.; Rabiei, S.; Yadav, R. T.; Hajaligol, M. R. *Appl. Catal., B* **2003**, *43*, 151.
- (30) Huang, X. H.; Chen, Z. H. *J. Magn. Magn. Mater.* **2004**, *280*, 37.
- (31) Chagas, P.; da Silva, A. C.; Passamani, E. C.; Ardisson, J. D.; de Oliveira, L. C. A.; Fabris, J. D.; Paniago, R. M.; Monteiro, D. S.; Pereira, M. C. *J. Nanopart. Res.* **2013**, *15*, 1544.
- (32) Gutierrez, L.; Gomez, L.; Irusta, S.; Arruebo, M.; Santamaria, J. *Chem. Eng. J.* **2011**, *171*, 674.